

LES for Prediction of Pressure Fluctuation for Supersonic Flow Around a Truncated Cone

**Shuh-Yi Chern
Greg Lobser
Michael Schoonmaker
Edward Heyd
Chaoqun Liu**

Technical Report 2014-15

LES for Prediction of Pressure Fluctuation for Supersonic Flow around a Truncated Cone

Shuh-Yi Chern, Greg Lobser, Michael Schoonmaker, Edward Heyd
MSS(Model, Simulation, and Software) group
ULA(United Launch Alliance)

Chaoqun Liu
University of Texas at Arlington

Abstract

In this study, we investigate the interaction between supersonic turbulence boundary layer and the shock wave induced by the flow past a circular truncated cone at $M=1.6$ and $Re=300,0000$. The UTA high order large eddy simulation code (LESUTA) with the 5th order Bandwidth-optimized WENO scheme is used to investigate the flow field structures and pressure fluctuation including the power spectrum of the noise caused by the supersonic turbulent boundary layer and shock interaction. The agreement between LES results and the experimental results are reasonable well. In addition, the three dimensional flow field especially at the separation region is illustrated.

I. Introduction

Shock Wave-Boundary Layer interaction (SWBLI) is a kind of problem which is frequently met in high-speed flight. It occurs in numerous external and internal flow problems relevant to aircraft and launch vehicles. The interactions usually decrease the total pressure recovery, degenerate the shape factor of the supersonic boundary layer, and result in flow separation.

There are many previous experimental¹⁻⁸ and numerical works⁹⁻¹⁹ study the supersonic ramp flow which is a typical prototype SBLI problem. According to their research, some flow mechanisms are recognized as: a) the amplification of the turbulence after the SWBLI is thought to be caused by the nonlinear interaction between the shock wave and the coupling of turbulence, vorticity and entropy waves²⁰; b) the unsteady motion of the shock is considered to be generated by the very long low-momentum coherent structures in logarithmic layer and such structures might be formed by the hairpin vortex packet.

Although there are many previous experimental and computational works on SWBLI problems, there still exist many issues to solve, such as the physical essence of the separation, the 3D and transient properties of turbulent boundary layer, the position of the peak of pressure and etc. In addition, the interaction between the separation and shock induced by a bluff body in supersonic flow should be another very important topic. The prediction of pressure fluctuation for separated supersonic turbulent boundary layer and shock interaction is also a challenge to numerical methods.

In this study, we try to understand the mechanism of the SWBLI for the flow over a bluff body. We investigate the interaction between supersonic turbulence boundary layer and the shock wave induced by the flow past the circular truncated cone at $M=1.6$ and $Re=300,0000$. In order to make simulations, a kind of large eddy simulation method is used by solving the

unfiltered form of the Navier-Stokes equations (NSEs) with the 5th order bandwidth-optimized WENO scheme, which is generally referred to the so-called implicitly implemented LES. The paper is arranged as follows: in section II, we give the information of case setup; in section III, the numerical methods we adopted in the LES are specified; in section IV, the results for two validation cases are presented; in section V, the numerical results are discussed in detail and compared to the experimental ones. Finally, we give our conclusions.

II. Case Setup and Grid Generation

2.1 Configuration and inflow condition

The computation case is specified based on the experiment work (Robertson) provided in Ref 21(Figure 1). Since our current code and only deal with parallel computation of fluid flow within one topologic block, the simplified computation case is simulated (Figure 2) where the cylinder is replaced by a circular truncated cone. The simplified case will be a typical 3-D domain. The dimensions and the flow parameters are given as follows:

The height of the circular truncated cone $h=8\text{in}$, the radius of the bottom and top surface are 8in and 4in respectively, the inf low boundary layer thickness is $\delta_0 = 0.1$. The mach number is $M_\infty=1.6$, the reference length is $L_{\text{ref}}=h$, the Reynolds number, Re/ft , has been increased to $300,0000$.

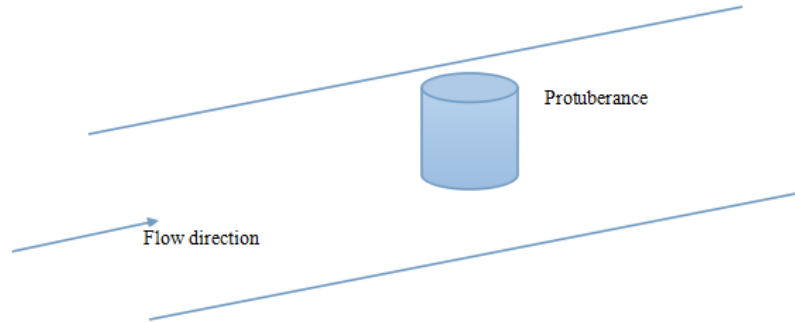


Figure 1. Sketch of the protuberance flow

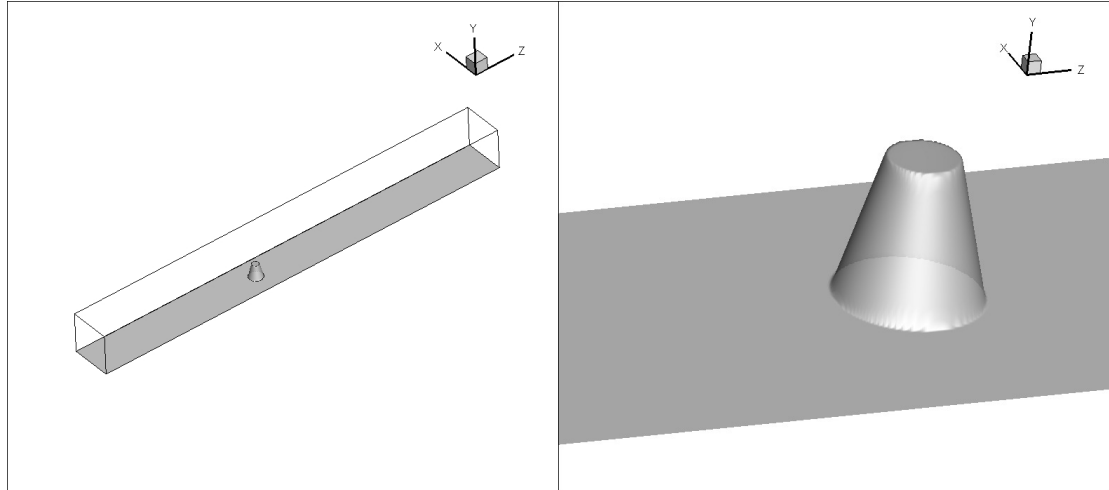


Figure 2. 3D domain of the flow field simulated

2.2 Grid generation

Orthogonal three dimensional grids (shown in Fig 3, at the step part) for the ramp flow domain have been generated with around 50 millions of grid points (1600x192x160 in the streamwise, normal, and spanwise directions).

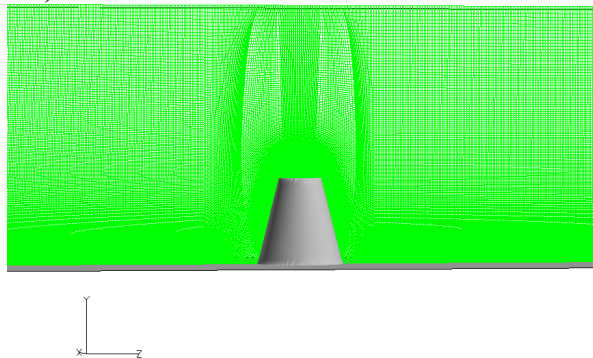


Figure 3. Flow passed 3-D truncated cone

III. Numerical Methods

The UTA high order large eddy simulation code (LESUTA) is used to investigate the flow field structures and pressure fluctuation including the instant and time averaged power spectrum of the noise caused by the supersonic turbulent boundary layer and shock interaction . The LES code was previously well validated for unsteady applications in a supersonic inviscid flow around a half cylinder at $M=4$ and an MVG controlling ramp flow at $M=2.5$ and $Re=5760^{22}$. The details of the numerical schemes used in LESUTA is specified as follows:

3.1 Governing Equations

The governing equations are the non-dimensional Navier-Stokes equations in conservative form as follows:

$$\frac{\partial Q}{\partial t} + \frac{\partial E}{\partial x} + \frac{\partial F}{\partial y} + \frac{\partial G}{\partial z} = \frac{\partial E_v}{\partial x} + \frac{\partial F_v}{\partial y} + \frac{\partial G_v}{\partial z}, \quad (1)$$

where

$$Q = \begin{bmatrix} \rho \\ \rho u \\ \rho v \\ \rho w \\ e \end{bmatrix} \quad E = \begin{bmatrix} \rho u \\ \rho u^2 + p \\ \rho uv \\ \rho uw \\ (e+p)u \end{bmatrix} \quad F = \begin{bmatrix} \rho v \\ \rho vu \\ \rho v^2 + p \\ \rho vw \\ (e+p)v \end{bmatrix} \quad G = \begin{bmatrix} \rho w \\ \rho wu \\ \rho wv \\ \rho w^2 + p \\ (e+p)w \end{bmatrix}$$

$$E_v = \frac{1}{\text{Re}} \begin{bmatrix} 0 \\ \tau_{xx} \\ \tau_{xy} \\ \tau_{xz} \\ u\tau_{xx} + v\tau_{xy} + w\tau_{xz} + q_x \end{bmatrix} \quad F_v = \frac{1}{\text{Re}} \begin{bmatrix} 0 \\ \tau_{yx} \\ \tau_{yy} \\ \tau_{yz} \\ u\tau_{yx} + v\tau_{yy} + w\tau_{yz} + q_y \end{bmatrix} \quad G_v = \frac{1}{\text{Re}} \begin{bmatrix} 0 \\ \tau_{zx} \\ \tau_{zy} \\ \tau_{zz} \\ u\tau_{zx} + v\tau_{zy} + w\tau_{zz} + q_z \end{bmatrix}$$

$$e = \frac{p}{\gamma-1} + \frac{1}{2} \rho(u^2 + v^2 + w^2) \quad q_x = \frac{\mu}{(\gamma-1)M_\infty^2 \text{Pr}} \frac{\partial T}{\partial x} \quad q_y = \frac{\mu}{(\gamma-1)M_\infty^2 \text{Pr}} \frac{\partial T}{\partial y}$$

$$q_z = \frac{\mu}{(\gamma-1)M_\infty^2 \text{Pr}} \frac{\partial T}{\partial z} \quad p = \frac{1}{\gamma M_\infty^2} \rho T \quad \text{Pr} = 0.72$$

$$\tau = \mu \begin{bmatrix} \frac{4}{3} \frac{\partial u}{\partial x} - \frac{2}{3} \left(\frac{\partial v}{\partial y} + \frac{\partial w}{\partial z} \right) & \frac{\partial u}{\partial y} + \frac{\partial v}{\partial x} & \frac{\partial u}{\partial z} + \frac{\partial w}{\partial x} \\ \frac{\partial u}{\partial y} + \frac{\partial v}{\partial x} & \frac{4}{3} \frac{\partial v}{\partial y} - \frac{2}{3} \left(\frac{\partial w}{\partial z} + \frac{\partial u}{\partial x} \right) & \frac{\partial v}{\partial z} + \frac{\partial w}{\partial y} \\ \frac{\partial u}{\partial z} + \frac{\partial w}{\partial x} & \frac{\partial v}{\partial z} + \frac{\partial w}{\partial y} & \frac{4}{3} \frac{\partial w}{\partial z} - \frac{2}{3} \left(\frac{\partial u}{\partial x} + \frac{\partial v}{\partial y} \right) \end{bmatrix}$$

The dynamic viscosities coefficient is given by Sutherland's equation:

$$\mu = T^{\frac{3}{2}} \frac{1+C}{T+C}, \quad C = \frac{110.4}{T_\infty} \quad (2)$$

The non-dimensional variables are defined as follows:

$$x = \frac{\tilde{x}}{L}, y = \frac{\tilde{y}}{L}, z = \frac{\tilde{z}}{L}, u = \frac{\tilde{u}}{U_\infty}, v = \frac{\tilde{v}}{U_\infty}, w = \frac{\tilde{w}}{U_\infty},$$

$$T = \frac{\tilde{T}}{T_\infty}, \mu = \frac{\tilde{\mu}}{\mu_\infty}, k = \frac{\tilde{k}}{k_\infty}, \rho = \frac{\tilde{\rho}}{\rho_\infty}, p = \frac{\tilde{p}}{\rho_\infty U_\infty^2}, e = \frac{\tilde{e}}{\rho_\infty U_\infty^2}$$

where the variables with '~' are the dimensional counterparts.
Considering the following grid transformation,

$$\begin{cases} \xi = \xi(x, y, z) \\ \eta = \eta(x, y, z) \\ \zeta = \zeta(x, y, z) \end{cases} \quad (3)$$

the Navier-Stokes equations can be transformed to the system using generalized coordinates:

$$\frac{\partial \hat{Q}}{\partial \tau} + \frac{\partial \hat{E}}{\partial \xi} + \frac{\partial \hat{F}}{\partial \eta} + \frac{\partial \hat{G}}{\partial \zeta} = \frac{\partial \hat{E}_v}{\partial \xi} + \frac{\partial \hat{F}_v}{\partial \eta} + \frac{\partial \hat{G}_v}{\partial \zeta} \quad (4)$$

where $\hat{Q} = J^{-1}Q$ and

$$\hat{E} = J^{-1}(\xi_x E + \xi_y F + \xi_z G) \quad \hat{F} = J^{-1}(\eta_x E + \eta_y F + \eta_z G) \quad \hat{G} = J^{-1}(\zeta_x E + \zeta_y F + \zeta_z G)$$

$$\hat{E}_v = J^{-1}(\xi_x E_v + \xi_y F_v + \xi_z G_v) \quad \hat{F}_v = J^{-1}(\eta_x E_v + \eta_y F_v + \eta_z G_v) \quad \hat{G}_v = J^{-1}(\zeta_x E_v + \zeta_y F_v + \zeta_z G_v)$$

J^{-1}, ξ_x , etc are grid metrics, and $J^{-1} = \det\left(\frac{\partial(x, y, z)}{\partial(\xi, \eta, \zeta)}\right)$, $\xi_x = J(y_\eta z_\zeta - z_\eta y_\zeta)$, etc.

3.2 Finite difference schemes and boundary conditions

3.2.1 The 5th order Bandwidth-optimized WENO scheme for the convective terms

For integrity, the 5th order WENO²³ will be described as follows. Considering the one dimensional hyperbolic equation:

$$\frac{\partial u}{\partial t} + \frac{\partial f(u)}{\partial x} = 0 \quad (5)$$

The semi-discretized equation can be expressed as:

$$\left(\frac{\partial u}{\partial t}\right)_j = -\frac{h_{j+1/2} - h_{j-1/2}}{\Delta x} \quad (6)$$

Considering the positive flux, the four upwind-biased schemes on three candidates can be given as:

$$\begin{cases} h'^+_0 = \frac{1}{3}f_{j-2} - \frac{7}{6}f_{j-1} + \frac{11}{6}f_j \\ h'^+_1 = -\frac{1}{6}f_{j-1} + \frac{1}{3}f_j + \frac{5}{6}f_{j+1} \\ h'^+_2 = \frac{1}{3}f_j + \frac{5}{6}f_{j+1} - \frac{1}{6}f_{j+2} \\ h'^+_3 = \frac{11}{6}f_{j+1} - \frac{7}{6}f_{j+2} + \frac{1}{3}f_{j+3} \end{cases} \quad (7)$$

The mark ‘+’ refers to the positive flux after flux splitting. 3rd order is obtained for each individual scheme. Schemes on basic stencils are symmetric to the one with respect to $x_{j+1/2}$.

Weighting and the linear weights to obtain higher order:

$$h^+_{Linear, j+1/2} = \alpha_0 h'^+_0 + \alpha_1 h'^+_1 + \alpha_2 h'^+_2 + \alpha_3 h'^+_3$$

The optimal order (Order optimized) for the weighted scheme is at most $2r$, where r is the number of the stencil. And when the optimal order is realized, the α_i must be determined as:

$$(\alpha_0, \alpha_1, \alpha_2, \alpha_3) = (0.05, 0.45, 0.45, 0.01).$$

The order of the scheme is 5th order.

The final nonlinear weighted schemes can be expressed as:

$$h^+_{j+1/2} = \omega_0 h'^+_0 + \omega_1 h'^+_1 + \omega_2 h'^+_2 + \omega_3 h'^+_3$$

where ω_i is changing from place to place, and

$$\begin{aligned} \omega_i &= b_i / (b_0 + b_1 + b_2 + b_3), \\ b_i &= \alpha_i / (\varepsilon + IS_i)^2 \end{aligned}$$

and ε is a small quantity ($10^{-6} \sim 10^{-10}$) to prevent the denominator from being zero, which should be small enough in supersonic problems with shocks. IS_i is the smoothness measurement.

In order to make the nonlinear scheme still pertain the same optimal order, i.e., 5th order, IS_i should have the property:

$$IS_k = C(1 + O(h^2))$$

where C is the same number for all four IS_i .

IS_i has the following form:

$$\begin{cases} IS_0 = \frac{13}{12}(f_{j-2} - 2f_{j-1} + f_j)^2 + \frac{1}{4}(f_{j-2} - 4f_{j-1} + 3f_j)^2 \\ IS_1 = \frac{13}{12}(f_{j-1} - 2f_j + f_{j+1})^2 + \frac{1}{4}(f_{j-1} - f_{j+1})^2 \\ IS_2 = \frac{13}{12}(f_j - 2f_{j+1} + f_{j+2})^2 + \frac{1}{4}(3f_j - 4f_{j+1} + f_{j+2})^2 \\ IS_3 = \frac{13}{12}(f_{j+1} - 2f_{j+2} + f_{j+3})^2 + \frac{1}{4}(-5f_{j+1} + 8f_{j+2} - 3f_{j+3})^2 \end{cases} \quad (8)$$

In order to make the scheme stable, further modification is made as: $IS_3 = \max_{0 \leq k \leq 3} IS_k$.

Further improvement for ω_k by Martin et al is:

$$\omega_i = \begin{cases} \alpha_k & \text{if } \max(TV_k) / \min(TV_k) < 5 \text{ and } \max(TV_k) < 0.2 \\ \omega_i & \text{otherwise} \end{cases} \quad (9)$$

where TV_k stands for the total variation on each candidate stencil.

The scheme for $h_{j+1/2}^-$ has a symmetric form of $h_{j+1/2}^+$ to the point $x_{j+1/2}$.

The large eddy simulation based on the WENO scheme was thought to be slightly more dissipative than other implicit LES methods. In order to decrease the dissipation of the scheme, the less dissipative Steger-Warming flux splitting method is used in the computation, not the commonly-used more dissipative Lax-Friedrich splitting method.

3.2.2 The difference scheme for the viscous terms

Considering the conservative form of the governing equations, the traditional 4th order central scheme is used twice to compute the 2nd order derivatives in viscous terms.

3.2.3 The time scheme

The basic methodology for the temporal terms in the Navier-Stokes equations adopts the explicit 3rd order TVB-type Runge-Kutta scheme :

$$\begin{aligned} u^{(1)} &= u^n + \Delta t L(u^n) \\ u^{(2)} &= \frac{3}{4}u^n + \frac{1}{4}u^{(1)} + \frac{1}{4}\Delta t L(u^{(1)}) \\ u^{n+1} &= \frac{1}{3}u^n + \frac{2}{3}u^{(2)} + \frac{2}{3}\Delta t L(u^{(2)}) \end{aligned} \quad (10)$$

3.2.4 Boundary conditions

The adiabatic, zero-gradient of pressure and non-slipping conditions are used for the wall as:

$$\partial T / \partial n = 0, \partial p / \partial n = 0, \vec{U} = 0 \quad (11)$$

To enforce the free stream condition, fixed value boundary condition with the free parameters is used on the upper boundary. No visible reflections are observed by the first shock. Even if there are reflections, the reflecting wave will go out of the domain into the inviscid region without entering the boundary layer and spoiling the computation. For the case of the ramp computation, the reflecting shock wave by SBLI is enclosed inside the domain. There is no unfavorable influence by the fixed value boundary condition. However, we need to change the far-field boundary condition to be non-reflecting in the next step of our work.

The boundary conditions at the front and back boundary surface in the spanwise direction are given as the mirror-symmetry condition. The reason is based on the assumption that the flow is assumed to be mirror-symmetric. In next step, we will change the spanwise boundary condition to be periodic.

The outflow boundary conditions are specified as a kind of characteristic-based condition, which can handle the outgoing flow without reflection. The details can be found in Reference²⁴.

3.2.5 Turbulent Inflow conditions

It is a challenging topic about how to get fully developed turbulent inflow comparable to the experimental conditions. There is a large body of published work on generating turbulent inflow boundary condition for simulation of complex spatially developing external flows; the most representative paper is perhaps that of Lund, Wu & Squires²⁵ developed a simplified version of the Spalart method by invoking only the transformation on independent variables at two streamwise stations without altering the Navier-Stokes equations. This method and its subsequent variations have been shown to yield reasonable inflow conditions for complex and spatially developed flows because quite often the downstream pressure gradients and geometrical variations mask any major defects of the inflow. However, because of their semi-empirical nature, even with DNS resolution, it would be quite challenging for these methods to generate results that can be considered as experimental data quality for the turbulent boundary layer. So, in present work, the turbulent mean profile and velocity fluctuations have been obtained from a separate DNS computation of compressible turbulent boundary layer.

The inflow conditions are generated using the following steps:

a) A turbulent mean profile is obtained from previous DNS simulation result from Ref. 26 for the streamwise velocity (w-velocity) and the distribution is scaled using the local displacement thickness and free stream velocity. The basic transfer is based on the assumption that the same distribution exists between the relations of $U/U_e \sim y/\delta^*$. And the averaged streamwise velocity of MVG case can be got by smooth interpolation (3rd spline interpolation).

b) The pressure is uniform at inlet and is the same as the free stream value. The temperature profile is obtained using Walz' s equation for the adiabatic wall:

First the adiabatic wall temperature is determined using: $T_w = T_e(1 + r(\gamma - 1)/2 \times M_e^2)$, where the subscript 'e' means the edge of the boundary layer and r is the recovery factor with value 0.9.

The temperature profile is obtained by Walz' s equation: $T/T_e = T_w/T_e - r(\gamma - 1)/2 \times M_e^2 (U/U_e)^2$.

c) The fluctuation components of the velocity are separated from the velocity at every instantaneous data file (total 20,000 files). And such fluctuations are rescaled in the same way. Because $\bar{T}/T_e = T_w/T_e - r(\gamma - 1)/2 \times M_e^2 (\bar{U}/U_e)^2$, considering the non-dimensional form and ignoring the T_e and U_e , we get $d\bar{T} = -r(\gamma - 1)M_e^2 U d\bar{U}$, or $\Delta T = -r(\gamma - 1)M_e^2 U \Delta U$. Density fluctuation is determined by $\frac{\Delta \rho}{\bar{\rho}} = -\frac{\Delta T}{\bar{T}}$.

d) Finally, the transformed parameters are $u = U + \Delta u$, $v = V + \Delta v$, $w = \Delta w$, $\rho = \bar{\rho} + \Delta \rho$, $p = \frac{\rho T}{\gamma M^2}$, $T = \bar{T} + \Delta T$.

Such inflow conditions are, of course, not the exact solutions of the Navier-Stokes equations. The flow solver will adjust and modulate the flow into fully developed turbulent flows while propagating downstream.

This is a difficult part of the LES simulation. First, we have to get a huge data set from our previous DNS for flow transition, which has 20,000 files to read. Second we have to run about 100,000 time steps for the turbulent inflow to pass the whole computational domain. This is a very CPU time consuming job.

We checked the inflow and confirmed that the inflow is fully developed turbulent. Fig 4. shows the inflow boundary layer velocity profile in log - coordinates. There is a well-defined log

region and the agreement with the analytic profile is well throughout. These results are typical for a naturally grown turbulent boundary layer in equilibrium.

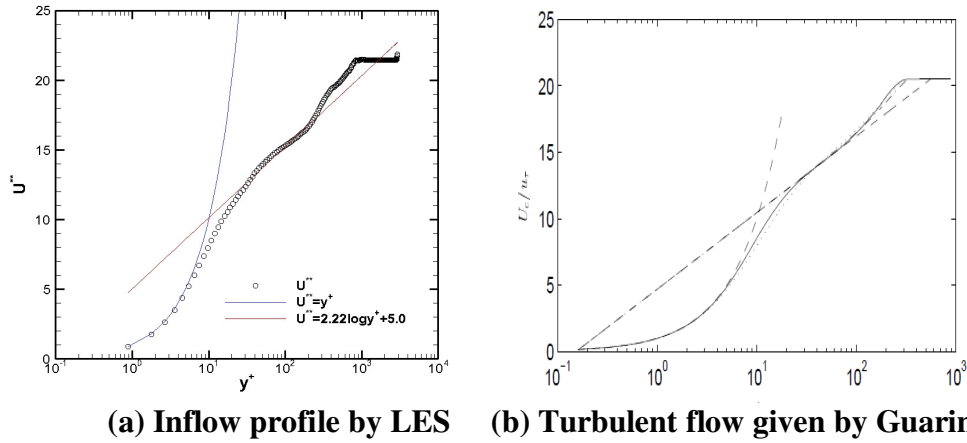


Figure 4. Turbulent inflow validation

IV. Validation

4.1 Micro vortex generator

The UTA high order LES code was developed under the support of US Air Force through an AFOSR grant. The code has been validated by UTA Aerodynamics Research Center and Delft University of Technology in Netherlands through 3-D PIV for supersonic flow around micro vortex generator (MVG) (see Figure 5) which is used to reduce the separation and pressure fluctuation induced by shock-boundary layer interaction. The agreement between experiment conducted by Delft and LES conducted by UTA is very well²⁸ (see Figures 6,7).

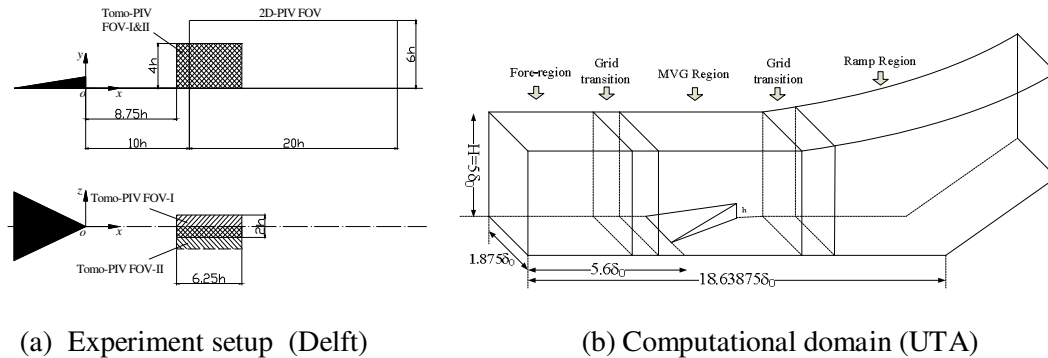


Figure 5. Les and experiment setup for micro vortex generator

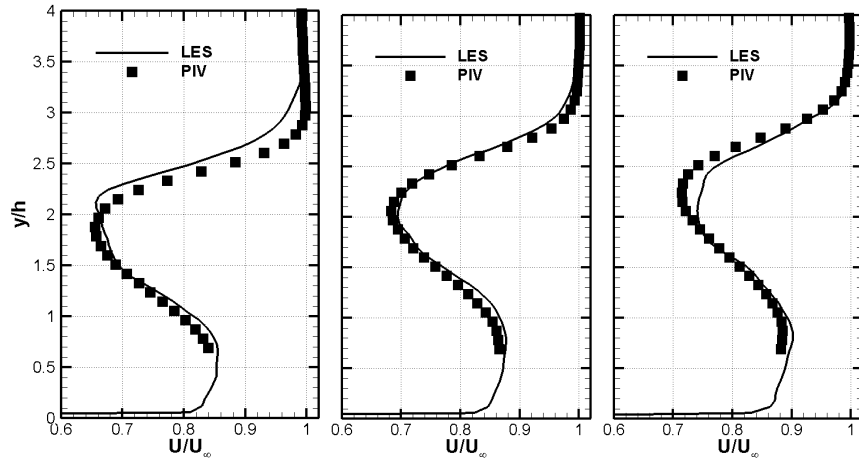


Figure 6. Profiles of u comparison in the center plane: (a) $x/h=10$ (b) $x/h=12$ (c) $x/h=14$.

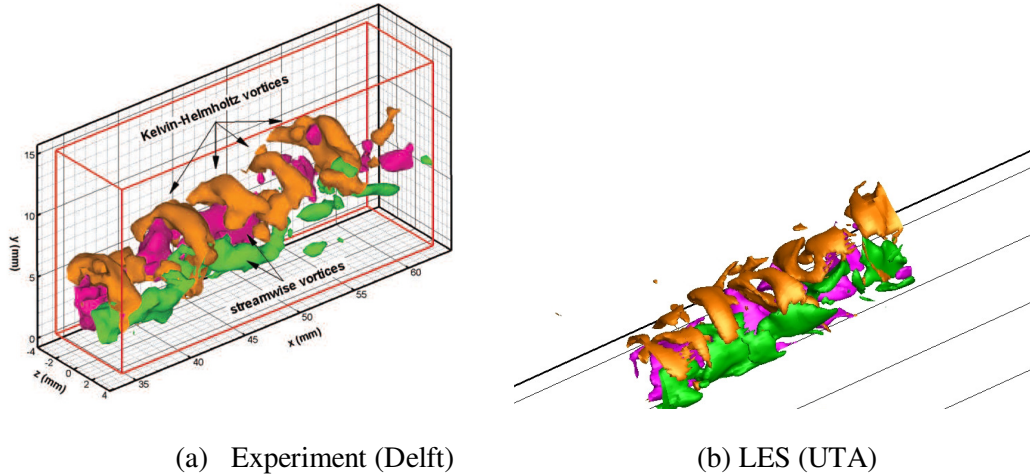


Figure 7. Comparison in vortex structure

4.2 Prediction of Pressure Fluctuation for Separated Supersonic Turbulent Boundary Layer and Shock Interaction

This case is to employ the UTA high order large eddy simulation code (LESUTA) to investigate the pressure fluctuation including the instant and time averaged power spectrum of the noise caused by the supersonic turbulent boundary layer and shock interaction (Figure8). The LES results must be validated first by comparison with experiment²⁹.

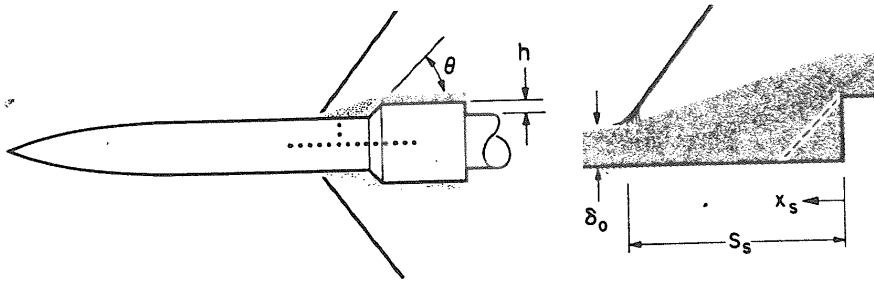
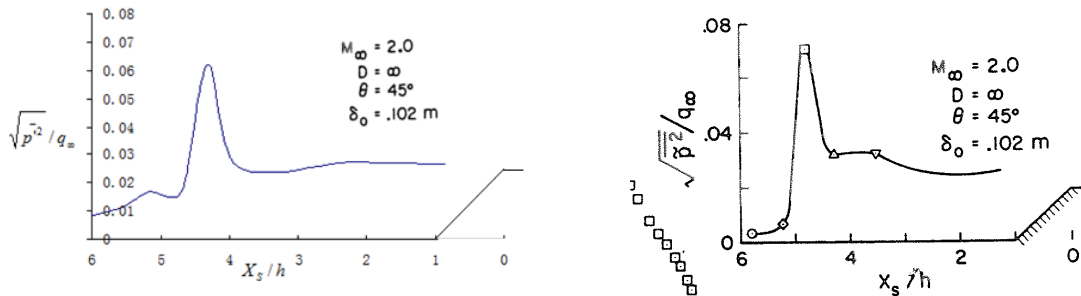


Figure 8. Shock and turbulence interaction around the ramp²⁹

The LES results have been compared with experiment²⁹ The time-averaged pressure distribution, $\frac{\sqrt{(p-p_{ave})^2}}{q_\infty}$ where q_∞ is the inflow dynamic pressure. In general, the agreement between our time-averaged LES results and the experimental results are reasonable well. Our LES successfully resolved the averaged pressure fluctuation distribution in the streamwise direction. There are only some discrepancies in comparison. The peak value of $\frac{\sqrt{(p-p_{ave})^2}}{q_\infty}$ is located at 0.44 in our LES, but 0.48 in experiment. The peak value is 0.064 in LES but 0.07 in experiment. The separation zone is about 4.8 obtained from Fig. 9a. which is smaller than the one by the experiment, that is about 5.0. The spectrum of pressure fluctuation induced by the boundary layer separation is also given in Fig. 10 which compare well with experiment.



(a) LES results

(b) Experimental results (AIAA 73-996)

Figure 9. Time-averaged pressure fluctuation in the central plane

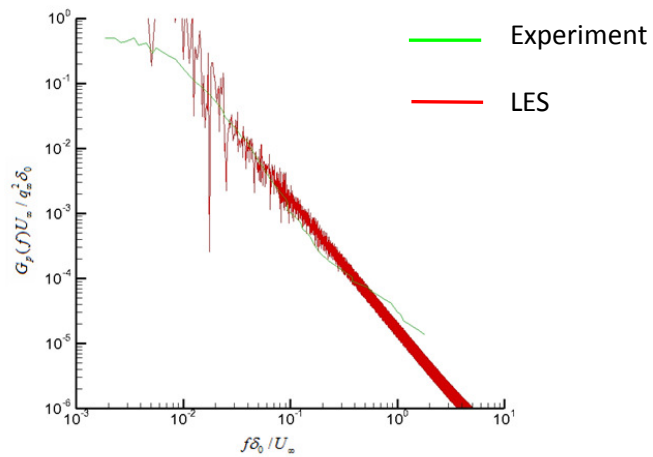


Figure 10 Power spectrum of shock induced pressure fluctuation

V. Numerical Result for Shock-boundary Layer Interaction around 3-D Cylinder

First we must validate our LES results by comparing the flow pattern of the protuberance flow field²¹ which is given in Fig. 11 and Fig. 12.

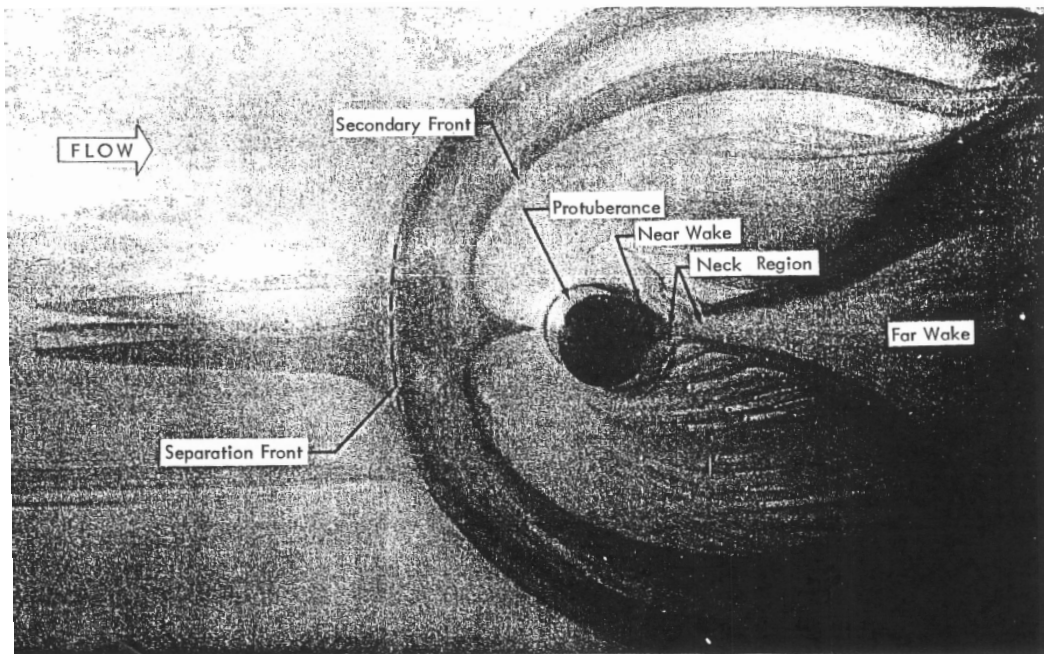


Figure 11. Experimental result of the flow pattern around the cylinder

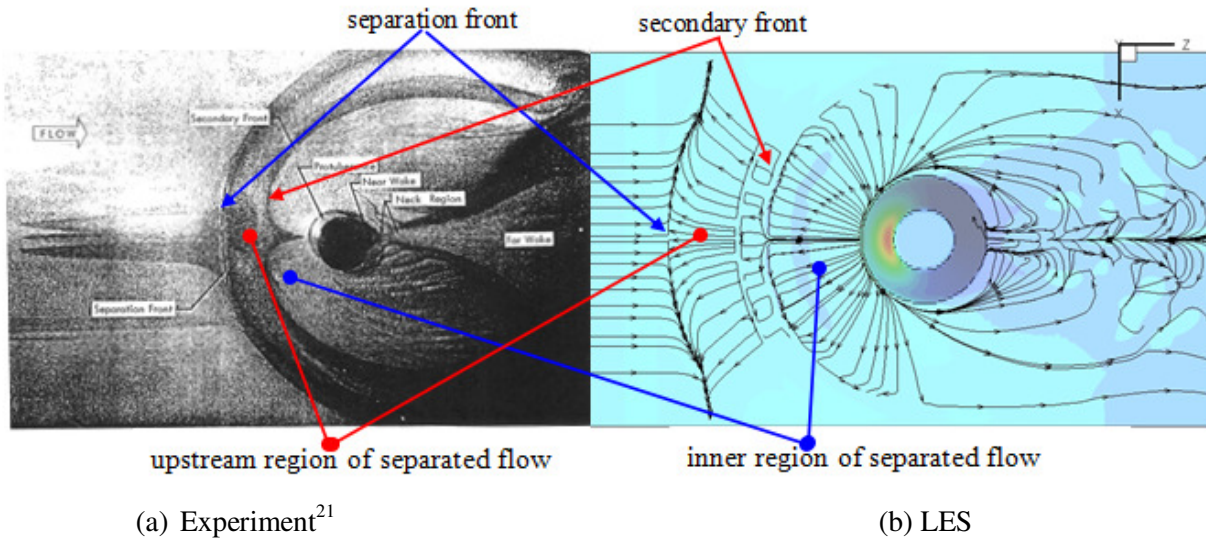


Figure 12. Comparison of flow structure around cone

In general, the agreement between our time-averaged LES results and the experimental results are reasonable well. However, there are still some discrepancies in comparison. The first and second separation front are both captured. Both the separated flow and wake regions are clearly shown in Figure 12. According to Ref 1, the separation line or front is parabolic in shape, the shape is well recovered by LES. The shape changes at two spanwise boundary since the computational domain is limited and boundary conditions must be applied. In comparison, the parabolic second front is in good agreement with the experiment. The separation length(see Figure 13) in experiment given by Ref 21 is about $1.95D$ (D is the radius of cylinder) at $M_\infty=1.6$ and it is $2.1D$ in our LES. The separation zone is a little larger than the one obtained by the experiment.

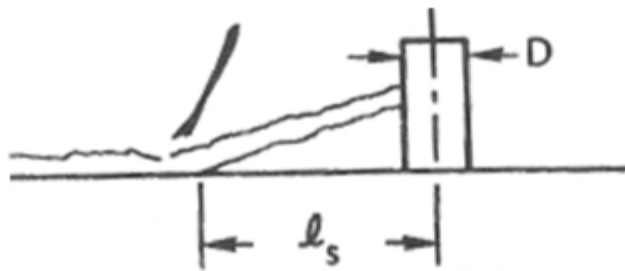


Figure 13. Sketch of the separation length

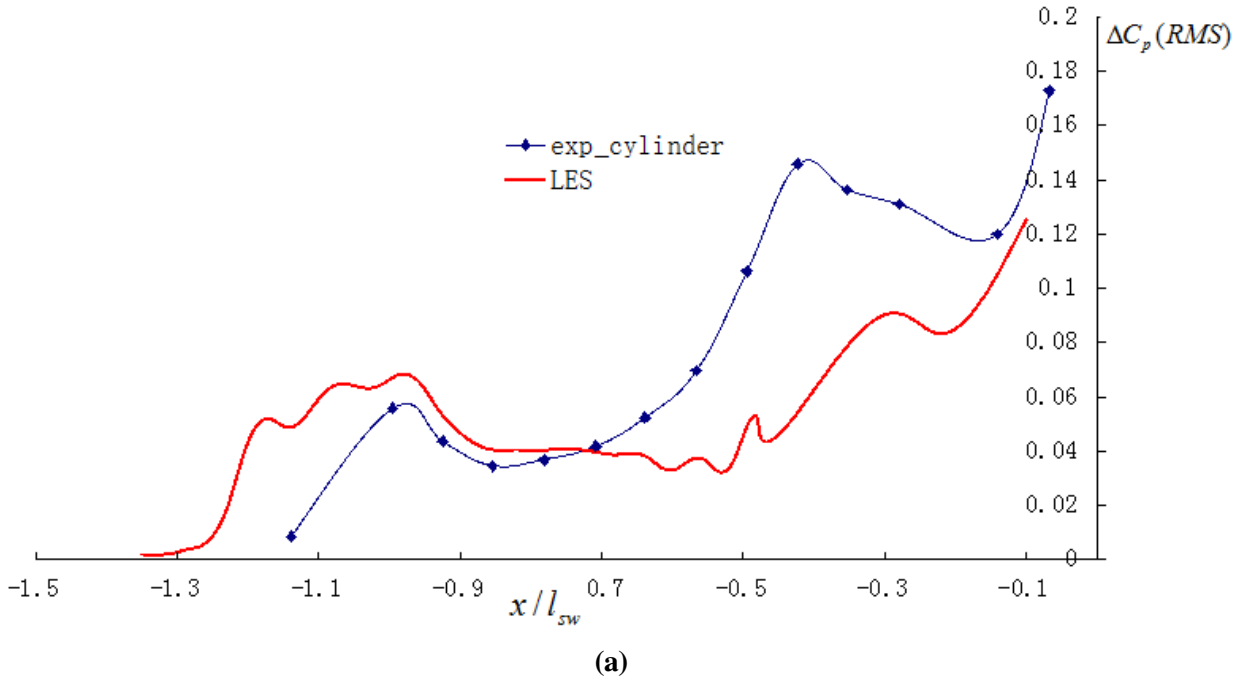
5.1 Pressure fluctuations and Power Spectra

From current data, we captured the pressure values with 28000 time steps for the flow field before separation and 20000 time steps in the downstream. The result show that the power spectra of pressure fluctuation at the shock position matches the profile from the experiment very well. There is some difference with the comparison between LES and experiment data the separated flow. These difference my induced by the different protuberance we put in the fluid field(circular truncated cone instead of

cylinder). While, the LES results show the ability to get the correct pressure fluctuations in the separation flow. However, the grid size for current LES simulation is too large to capture the turbulence properties for power spectra analysis with the constrains of time and computing consumption. To get the better result, we need refine the grid and apply DNS on the turbulence part. Also, it's hard to determine the turbulence intensity that is applied on the inlet which makes the difference in the power spectra at attached turbulent boundary layer since there are no such value mentioned in the experiment work.

5.2 Root-mean-square coefficient of the fluctuating pressure about the mean

In Fig.14, the Root-mean-square coefficient of the fluctuating pressure about the mean, $\Delta C_p(RMS) = \Delta P(RMS) / q_\infty$ is compared between the experiments and our LES. Basically, the distribution of $\Delta C_p(RMS)$ from LES keeps the same tendency with the result from experiment. The difference at the beginning is thought to be induced by the larger separation zone in our simulation. Fig. 15 shows the comparison of power spectra (pressure fluctuation) for shock-wave oscillation induce by two- and three-dimensional protuberances. The results from our LES match the experiment data very well.



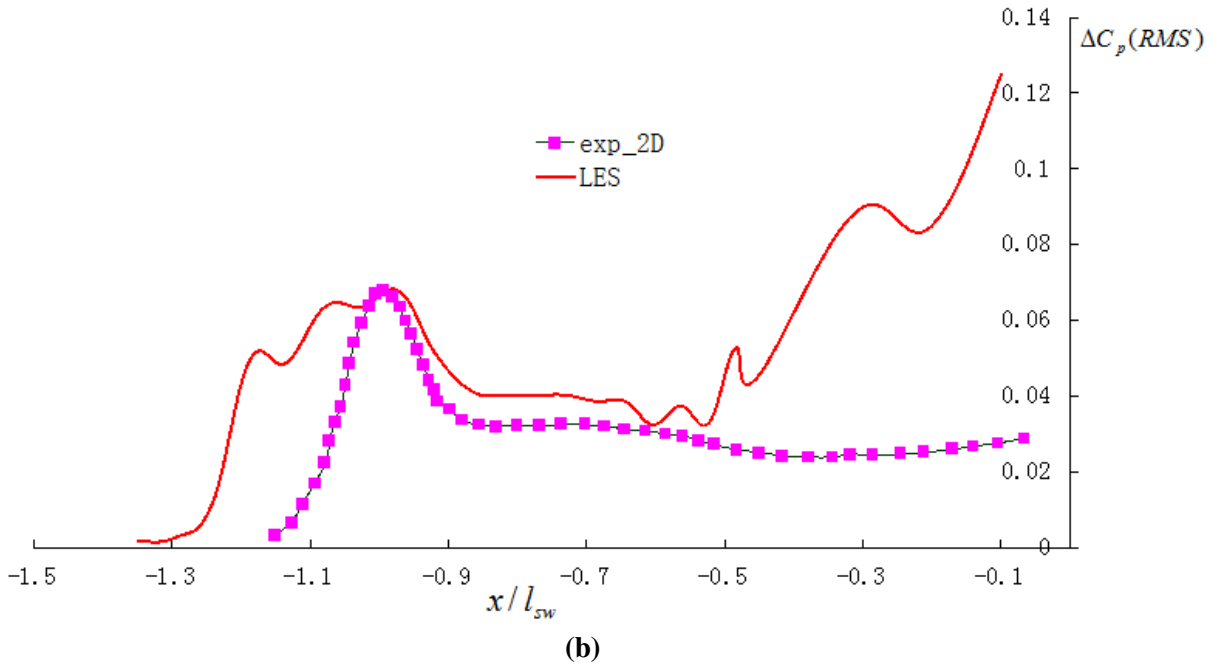


Figure 14. Comparison of Two- and Three-dimension separated flows(Root-mean-square coefficient of the fluctuating pressure). (a). Comparison with flow around circular cylinder from Ref 21. (b). Comparison with flow over 45° wedge at Ma=2.0 from Ref 21.

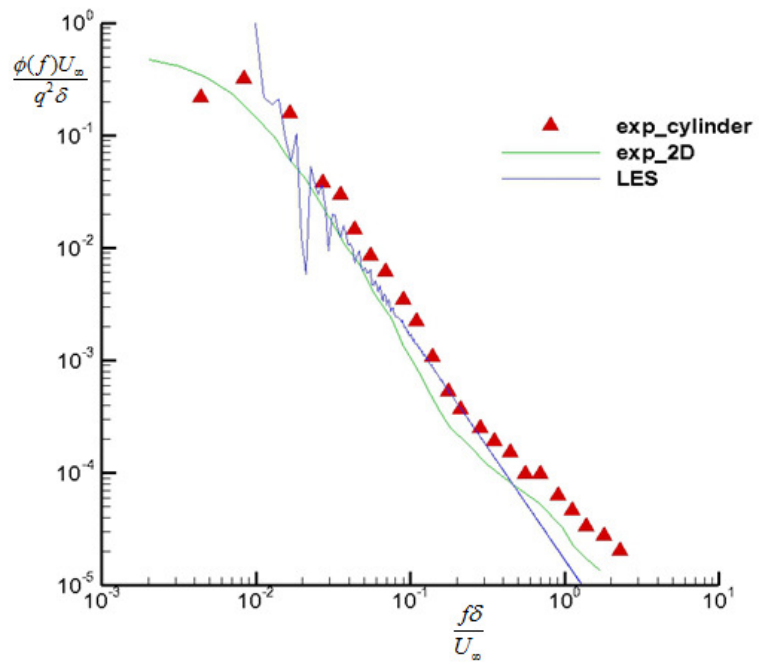


Figure 15. Comparison of power spectra for shock-wave oscillation induce by two- and three-dimensional protuberances

5.4 Properties of the Flow Field

In this part, we would like to provide some instantaneous and time-averaged flow field and give some analysis based on our observation.

5.4.1 Pressure and density gradient

Fig. 16 gives the pressure gradient distribution, Fig. 17 depicts the density gradient distribution in the flow, and Fig. 18 gives the 3D view of shock-waves around the protuberance which shows the complex structure for the shock–boundary layer interaction including the Λ -shape shock structure in the central plane. All of these shock waves and the induced separation flow could be the source of the pressure fluctuation and noise. Of course, the shock nearby the separation zone is the major source of the pressure fluctuation. Fig. 19 and 20 are the pressure distribution on the wall surface and central plane respectively. Apparently, the pressure is high nearby the front surface of the cone (blue means low and red means high).

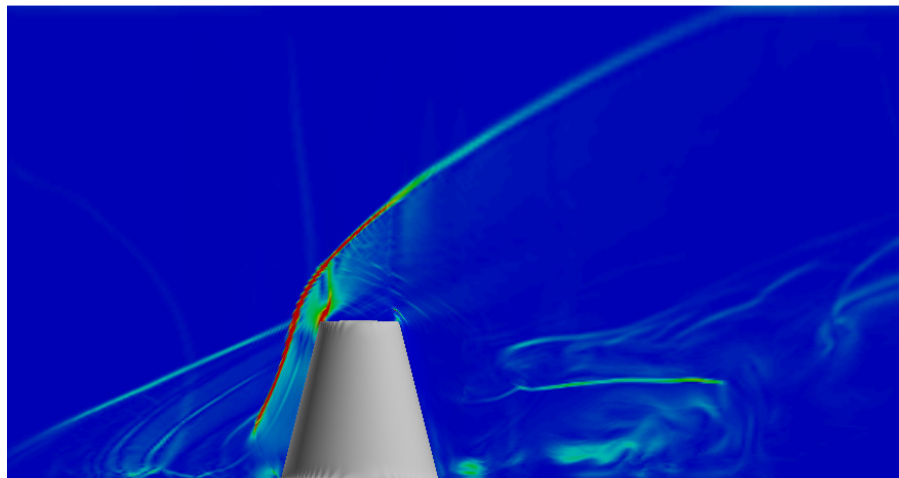


Figure 16. Pressure gradient at central plane and the corner

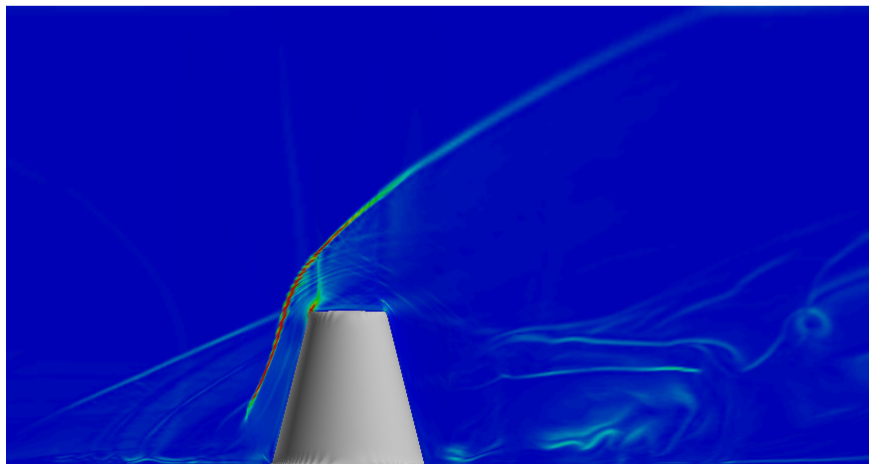


Figure 17. Density gradient at central plane and the corner

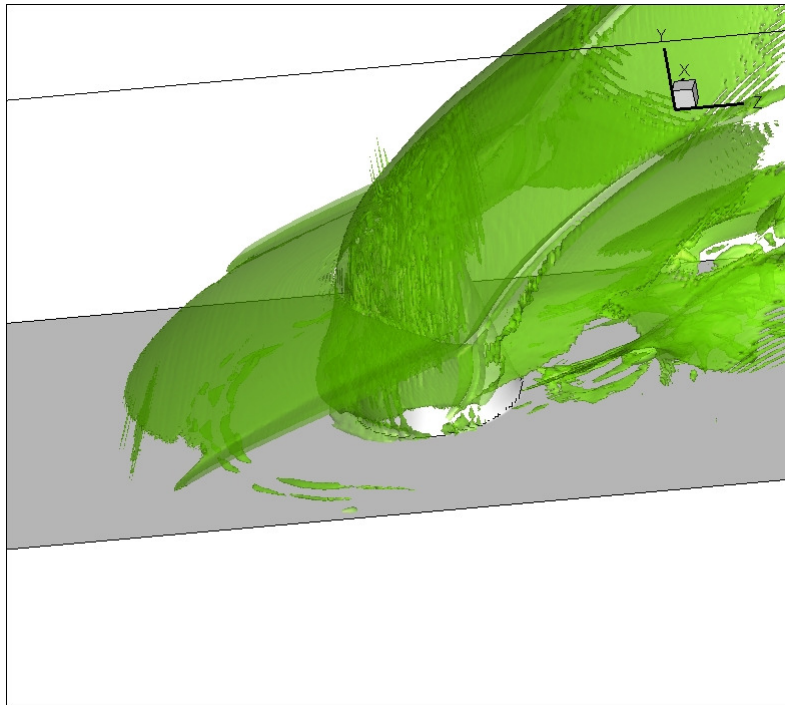


Figure 18. 3D shock by iso-surface of pressure gradient

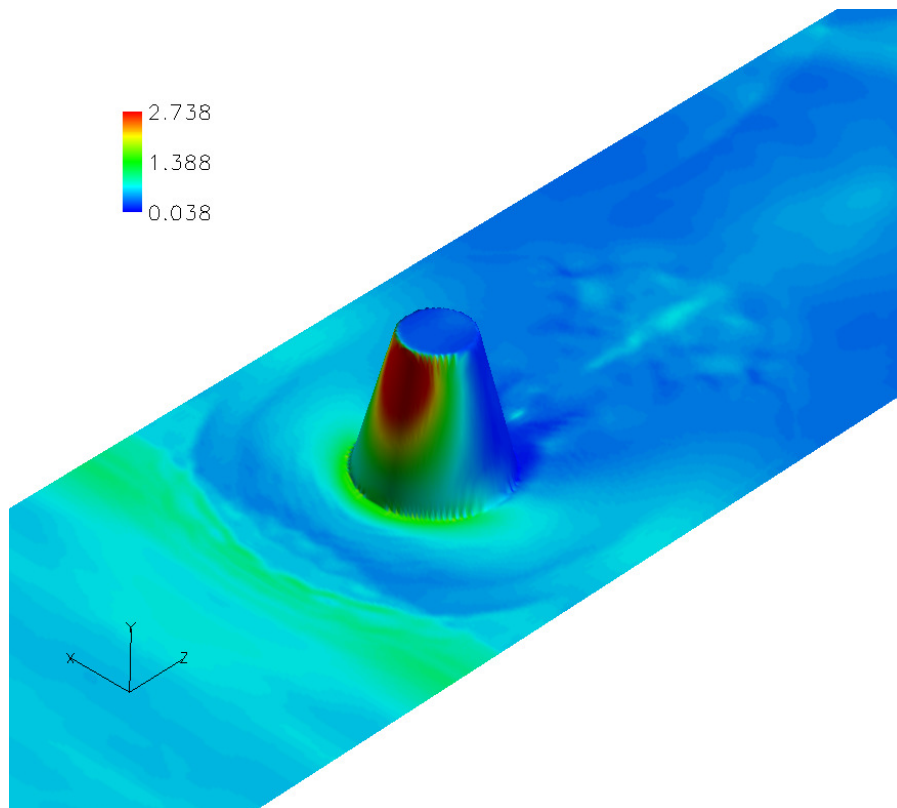


Figure 19. Pressure distribution on the wall

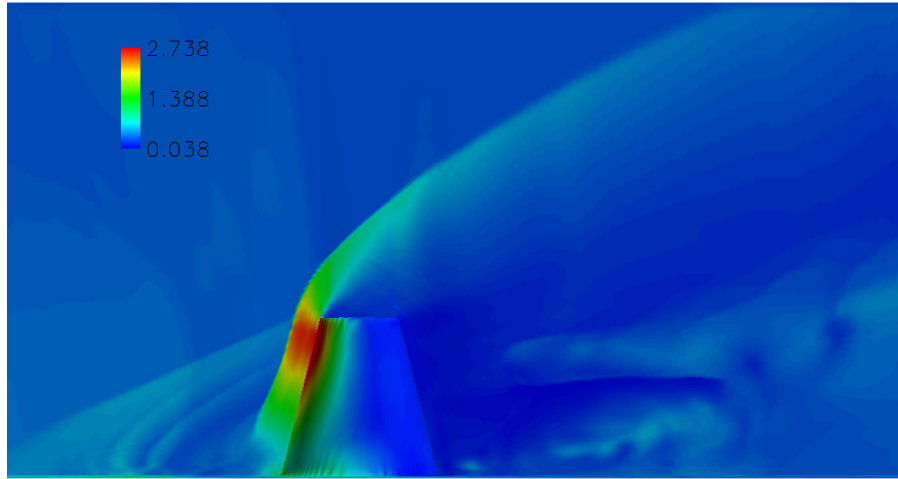
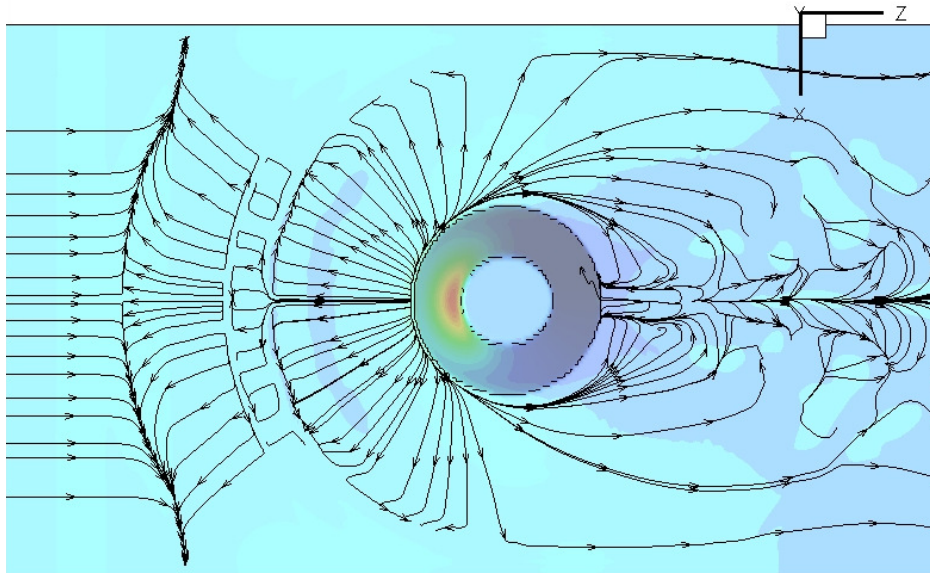


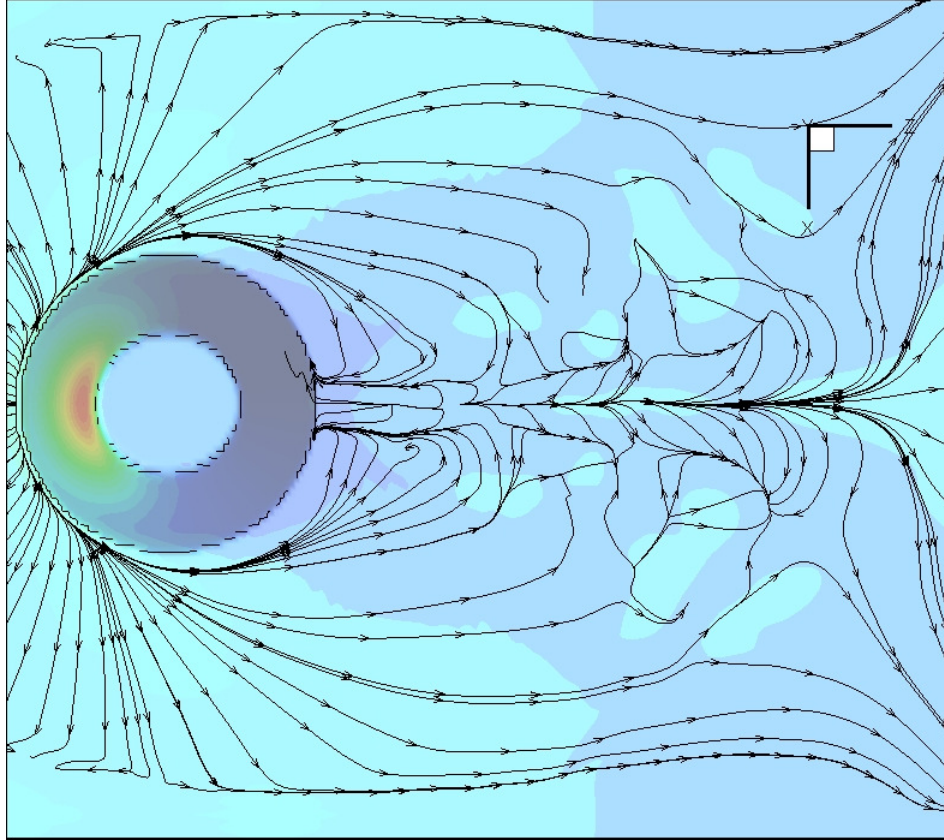
Figure 20. Pressure distribution on the central plane

5.4.2 Flow in separation zone

The shock-boundary layer interaction will cause the flow separation. Fig. 21 provides the stream track on the wall surface, which clearly shows the topology of shock induced separation zone. Fig. 22 gives the corresponding 3-D view of the stream track which is colored by local pressure distribution. As the vortices keep moving, the separation zone shape and size will keep changing as well. The separation zone size change could further push forward and pull backward the shock, which is the major reason why the separated boundary layer has much large pressure fluctuations and noises than the attached boundary layers.



(a) Stream trace of the separation zone



(b) Locally enlarged at the rake part
 Figure 21. 2-D stream track on the wall of the separation zone

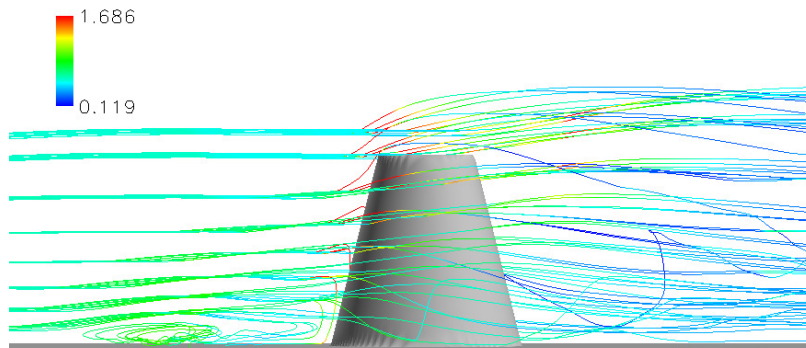


Figure 22. 3-D stream track of the separation zone (lines are colored by local pressure distribution)

5.4.3 Vortex structure

In order to investigate the vortex structure within and after the separation, a technique³⁰ is used by the iso-surface of the λ_2 , which is the second eigenvalue of the 3×3 matrix comprised of velocity gradient, i.e., $M_{ij} = \sum_{k=1}^3 (\Omega_{ik} \Omega_{kj} + S_{ik} S_{kj})$, where $S_{ij} = 1/2(\partial u_i / \partial x_j + \partial u_j / \partial x_i)$ and $\Omega_{ij} = 1/2(\partial u_i / \partial x_j - \partial u_j / \partial x_i)$. A small negative value is selected for visualization. It can be seen from Figures 16 and 17 that there are a large amount of vortices with various length scales in the concerned region, and many of them are streamwise vortices.

Moreover, hairpin vortices with ring-like head are found within the vortices. The weaker of the inflow vortices at the selected iso-surface value means that the intensity of the vortices is stronger in the separation zone. This provides an indirect proof of the amplification of the fluctuation by the flow separation.

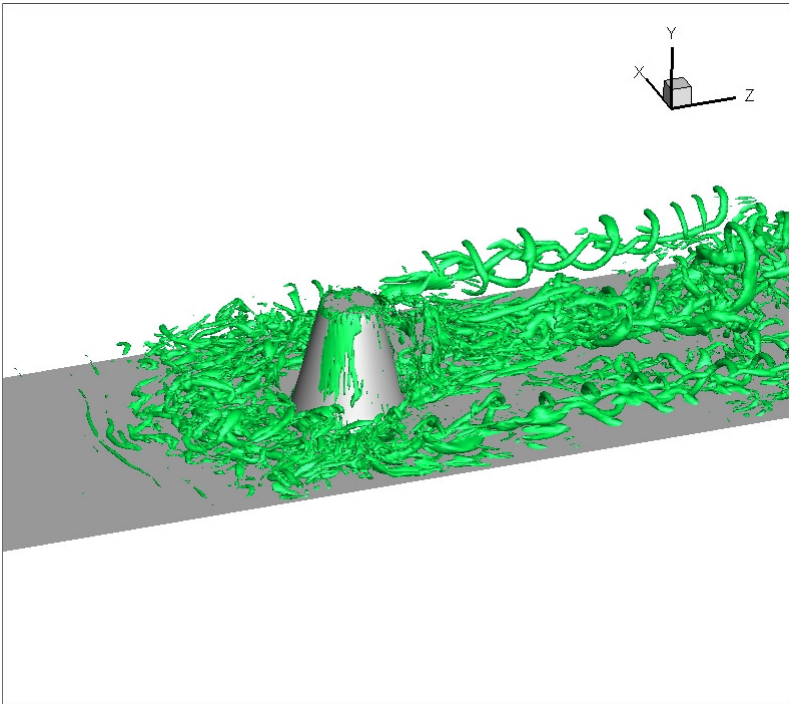


Figure 23. Vortex structure in the boundary layer shown by λ_2 (front view)

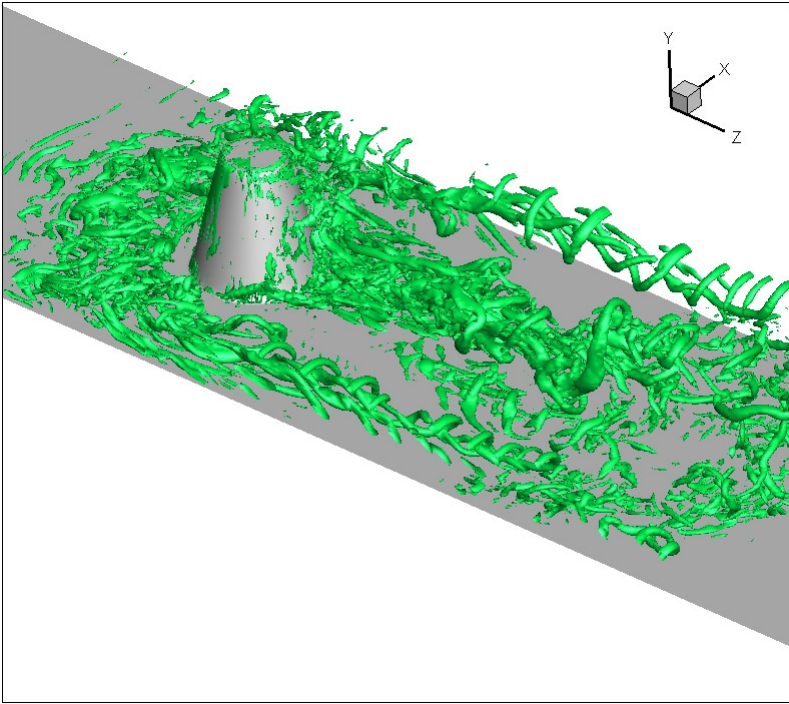


Figure 24. Vortex structure in the boundary layer shown by λ_2 (back view)

VI. Conclusion

The flow past a circular truncated cone is investigated by LES in this paper at $M=1.6$ and $Re=300,0000$. The UTA high order large eddy simulation code (LESUTA) with the 5th order Bandwidth-optimized WENO scheme is used to investigate the flow field structures and pressure fluctuation including the power spectrum of the noise caused by the supersonic turbulent boundary layer and shock interaction. The averaged pressure fluctuation distribution at the separation region, the pressure power spectra at the separation shock position are obtained. The agreement between time-averaged LES results and the experimental results from Ref 21 are reasonable well. The three dimensional flow field especially the vortex structure at the separation region is studied. It shows that there are a large amount of vortices with various length scales in the concerned region, and many of them are streamwise vortices. Moreover, hairpin vortices with ring-like head are found within the vortices.

References

- ¹Dolling, D. S., Murthy, M. T "Unsteadiness of the Separation Shock Wave Structure in a Supersonic Compression Ramp Flow field." *AIAA J.*, Vol. 12, pp.1628-1634(1983).
- ²Dolling, D. S. "High-Speed Turbulent Separated Flows: Consistency of Mathematic Models and Flow Physics." *AIAA J.*, Vol. 36, pp. 725-732(1998).
- ³Dolling, D. S. "Fifty Years of Shock-Wave/Boundary-Layer Interaction Research: What next?." *AIAA J.*, Vol. 39, pp. 1517-1531(2001).
- ⁴Settles, G. S. Dodson, L. J. "Supersonic and Hypersonic Shock/Boundary Layer Interaction Database." *AIAA J.*, Vol. 32, 1377-1383(1994).
- ⁵Dussauge, J. P., Dupont, P., Debieve, J. F. "Unsteadiness in Shock Wave Boundary Layer Interaction with Separation." *Aerospace Science and Technology*, Vol. 10, No. 2, pp.85-91(2006).
- ⁶Andreopoulos, J., Agui, J. H., Briassulis, G. "Shock Wave-Turbulence Interactions," *Annu. Rev. Fluid Mech.*, Vol. 32, pp.309-345(2000).
- ⁷Loginov, M. S., Adams, N. A., Zheltovodov, A. A. "Large-Eddy Eimulation of Shock-Wave/Turbulent-Boundary-Layer Interaction." *J. Fluid Mech.*, Vol. 565, pp. 135-169(2006).
- ⁸Wilcox, D., Turbulence Modeling for CFD, DCW Industries, Inc., 1993
- ⁹Zheltovodov, A. A. "Advances and Problems in Modeling of Shock Wave Turbulent Boundary Layer Interactions." *Proceedings of the international Conference on the Methods of Aerophysical research*, Institute of Theoretical and Applied Mechanics, Novosibirsk, Russia, pp.149-157(2004).
- ¹⁰Rizzetta, D., Visbal, M. "Large Eddy Simulation of Supersonic Compression-Ramp Flow by High-Order Method." *AIAA J.*, Vol. 39, No. 12, pp.2283-2292(2001).
- ¹¹Kaenel, R.V, Kleiser, L. Adams, N. A. Vos, J. B. "Large-Eddy Simulation of Shock-Turbulence Interaction." *AIAA J.*, Vol. 42, No. 12, pp.2516-2528(2004).
- ¹²Wu M. Martin, M. P. "Direct Numerical Simulation of Supersonic Turbulent Boundary Layer over a Compression Ramp." *AIAA J.*, Vol. 45, No. 4(2007).
- ¹³Adams, N. A."Direct simulation of the turbulent boundary layer along a compression ramp at $M = 3$ and $Re_\theta = 1685$." *J. Fluid Mech.*, Vol. 420, pp. 47-83(2000).
- ¹⁴Martín, M. P. "Direct Numerical Simulation of Hypersonic Turbulent Boundary Layers." Part 1. Initialization and Comparison with Experiments. *J. Fluid Mech.*, vol. 570, pp. 347–364(2007).
- ¹⁵Ringuette, M. Wu, M., Martín, M. P. "Low Reynolds Number Effects in a Mach 3 Shock/Turbulent-Boundary-Layer Interaction." *AIAA J.*, Vol. 46, No. 7, pp.1884-1887(2008).

- ¹⁶Wu, M., Martín, M. P. "Analysis of Shock Motion in Shockwave and Turbulent Boundary Layer Interaction Using Direct Numerical Simulation Data." *J. Fluid Mech.*, Vol. 594, pp. 71–83(2008).
- ¹⁷Ringuette, M. J. Wu, M., Martín, M. P. "Coherent Structures in Direct Numerical Simulation of Turbulent Boundary Layers at Mach 3." *J. Fluid Mech.*, vol. 594, pp. 59–69(2008).
- ¹⁸Priebe, S. Wu, M., Martín, M. P. "Direct Numerical Simulation of a Reflected-Shock-Wave/Turbulent-Boundary-Layer Interaction." *AIAA J.*, Vol. 47, No. 5, pp.1173-1185(2009).
- ¹⁹Bookey, P. Wyckham, C., Smits, A. "Experimental Investigations of Mach 3 Shock-Wave Turbulent Boundary Layer Interactions." *AIAA Paper 2005-4899*, 2005.
- ²⁰Smits, A. J., Dussauge, J. P. "*Turbulent Shear Layers in Supersonic Flow*," 2nd ed., Springer Verlag, New York(2006).
- ²¹J.E.Robertson, Fluctuating pressures induced by three-dimensional protuberance, Wyle Laboratories-research staff, Report WR 70-10.
- ²²Y. Yan, Q. Li, C. Liu et al., "*Numerical discovery and experimental confirmation of vortex ring generation by microramp vortex generator*", *Appl. Math. Modell.* (2012), doi:10.1016/j.apm.2012.01.015
- ²³Wu M. Martin, M. P. "Direct Numerical Simulation of Supersonic Turbulent Boundary Layer over a Compression Ramp." *AIAA J.*, Vol. 45, No. 4(2007).
- ²⁴Q. Li and C. Liu, LES for Supersonic Ramp Flow Control Using MVG at M=3 and Re=2400 AIAA Paper Number 2010-592, 2010
- ²⁵Lund, T. S., Wu, X., Squires, K. D. :Generation of turbulent inflow data for spatially developing boundary layer simulations. *J. Comput. Phys.* 140, 233 – 258(1998).
- ²⁶Liu C. and Chen, L.,:Study of Mechanism of Ring-Like Vortex Formation in Late Flow Transition. AIAA Paper 2010-1456.
- ²⁷Guarini, S. E.; Moser, R. D.; Shariff, K; Wray, A. , "Direct numerical simulation of a supersonic turbulent boundary layer at Mach 2.5". *Journal of Fluid Mechanics*, vol. 414, Issue 01, 2000, pp.1-33
- ²⁸Yonghua Yan, Xiao Wang, Chaoqun Liu. LES and Analyses on the Vortex Structure behind Supersonic MVG with Turbulent Inflow. *Appl. Math. Modell.* (2013), <http://dx.doi.org/10.1016/j.apm.2013.05.048>
- ²⁹C.F.Coe, W.J.Chyu and J.B.Dods,Jr. "*Pressure Fluctuations Underlying Attached and Separated Supersonic Turbulent Boundary Layers and Shock Waves*, AIAA paper,73-996.
- ³⁰J. Jeong, F. Hussain, On the identification of a vortex, *J. Fluid Mech.* 285 (1995) 69 – 94.